Multiscale computational models for the simulation of concrete materials and structures

5 authors, including:

Gianluca Cusatis
Northwestern University
123 PUBLICATIONS   **1,898** CITATIONS

SEE PROFILE

Roozbeh Rezakhani
École Polytechnique Fédérale de Lausanne
10 PUBLICATIONS   **94** CITATIONS

SEE PROFILE

Mohammed Alnaggar
Rensselaer Polytechnic Institute
25 PUBLICATIONS   **140** CITATIONS

SEE PROFILE

Xinwei Zhou
ES3
9 PUBLICATIONS   **73** CITATIONS

SEE PROFILE

Some of the authors of this publication are also working on these related projects:

Multi-physics modeling of concrete aging and deterioration View project

Multiscale Computational Framework for Analysis and Design of Ultra-High Performance Concrete Structural Components and Systems
View project

Multiscale computational models for the simulation of concrete materials and structures

G. Cusatis, R. Rezakhani & M. Alnaggar
Department Civil and Environmental Engineering, Northwestern University, Evanston, IL, USA

X. Zhou & D. Pelessone
MARS Department, ES3, San Diego, CA, USA

ABSTRACT: Concrete is a very complex multiscale material whose behavior at the engineering scale is strongly influenced by the heterogeneous character of its internal material structure. This paper provides an overview of the main features of various length scales in concrete and introduces three multiscale approaches—coarse-graining, bridging scale method, and mathematical homogenization—that can be used to upscale the Lattice Discrete Particle Model (LDPM). LDPM is a meso-scale discrete model that simulates the mechanical behavior of concrete by describing fracture and failure at the scale of coarse aggregate pieces. The efficiency of the presented multiscale methods is presented with reference to numerical examples that include the analysis of reinforced concrete shear walls; wave propagation; and alkali-silica-reaction induced expansion.

1 INTRODUCTION

Reinforced concrete structures are multiscale systems in which a large variety of length and time scales can be identified. This paper focuses solely on the discussion of multiple spatial scales, as per the pictorial representation shown in Figure 1, leaving the discussion of temporal scales to future work. Scale *I* is the largest scale, the scale of the full structure or, as typically referred to in the literature, the macroscopic engineering scale. Characteristic lengths of Scale *I* go from meters to tens of meters, for small to medium size structures such as buildings, urban overpasses, foundations, etcetera; and up to hundreds of meters for large structures such as, long-span bridges, skyscrapers, and dams. The analysis of Scale *I* is typically done through well established structural theories implemented in robust and computationally efficient software. These theories require knowledge of the behavior of each structural element—beams, columns, connections, etcetera—composing the structure. The structural element scale is Scale *II* in Figure 1 and it is characterized by lengths in the order of tens to hundreds of centimeters. Reinforced concrete elements consist of concrete and steel reinforcement in the form of rebars, prestressed strands and cables, stirrups, and other type of steel detailing. At this scale the mechanical behavior can be described by simulating concrete as a statistically homogeneous and isotropic quasi-brittle continuum; steel as an elasto-plastic continuum; and the concrete-steel

interface as a third "material" chracterized by its own peculiar properties. Formulation of appropriate constitutive equations at Scale *II* depends on the appropiate mathematical description of deformation and failure mechanisms that are often identified through laboratory experiments on samples whose size is in the order of few to several centimeters—see the plain concrete scale (Scale *III*) in Figure 1. For many decades, researchers have tried to formulate continuum costitutive equations for plain concrete but these attempts, although successful in many ways, failed to capture to the full extent the most important aspect of concrete behavior characterized by cracking and fracture. Fracturing behavior is strongly influenced by its heterogeneous internal structures. At the mesoscale (Scale *IV* in Fig. 1) concrete is considered a two-phase composite in which hard and stiff inclusions, the coarse aggregate particles (several millimeters to few centimeters large in standard concrete), are embedded in a softer and weaker mortar matrix. Modeling the effect of the major material heterogeneities is instrumental in order to capture the intrinsic material characteristic length associated with fracture and the consequent reduction of the structural strength as function of the structural size—the so-called Size Effect (Bažant and Planas 1998). At the mortar scale, also called concrete mini-scale (Cusatis et al. 2011) and indicated as Scale *V* in Figure 1, concrete can be regarded as a three-phase composite composed of (1) a porous matrix, the cement paste; (2) aggregate particles of all size (from several microns
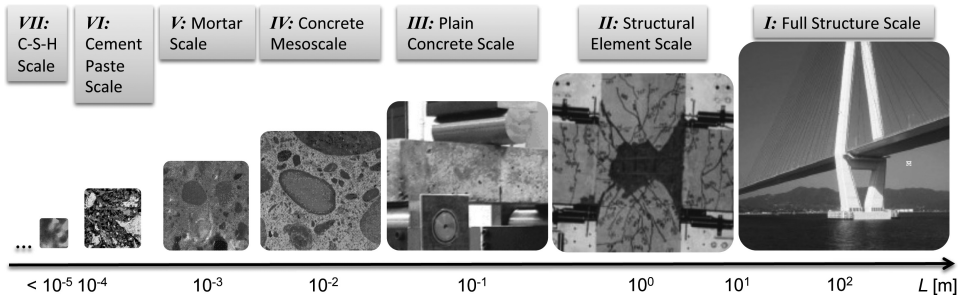
Figure 1. Concrete length scales.

to few centimeters in standard concrete); and (3) a thin layer (size of several microns) of material at the interface between cement paste and aggregate pieces, the so-called Interfacial Transition Zone (ITZ), which has distinctly different properties compared to the cement paste bulk. Scale *VI* is the scale of cement paste and ITZ whose internal structure features a very complex system of pores with size spanning various orders of magnitude (from nanometers to millimiters). At this scale, the internal structure and mineral composition of aggregate play a role also; this issue, however, is beyond the scope of this paper.

The six concrete scales described above are not the only ones: multiple other fine scales can be defined all the way down to the atomic structure. In one of the keynote papers presented at FraMCoS-6 conference (Emery et al. 2007), the keynote speaker says "[...] 40 years ago when the crew of the Star Ship Voyager used their handheld portable communicators to talk to anyone in the galaxy, who would have believed that today every student roaming a college campus would be carrying a wireless telephone? Will we be able to model every atom in a concrete structure 40 years from now? Definitely not, if we dont try". Probably it will take more than 40 years (actually a lot more) to make this vision a reality but there is no question that significant advancements in concrete mechanics will only come from looking at concrete from the perspective of its multiple length scales.

The formulation of a multiscale computational framework requires three fundamental ingredients: (1) A mathematical model describing the behavior of interest at a certain given scale; (2) Experimental data (not necessarily at the same scale of the selectedmodel) for calibration—identification of model parameters—and validation—proof of predictive capability; and (3) multiscale theories and technologies allowing the upscaling of the selected model to Scale *I*.

Where should we start? In ancient times structures were built "sine scienzia"—without

science—and structural design relied completely on the experience and intuition of *engineers* and *architects* whose source of knowledge was simply the knowledge transfered from their senior mentors. For this reason structures would collapse multiple time during construction and after each collapse the design would be adjusted accordingly to the observation of the collapse causes. As a result building a momument would take hundres of years and would be extremely expensive. By all means these design practices consisted in Scale *I* experimental tests; tests of the full structure. For obvious reasons, Scale *I* tests are unthinkable in modern times in civil engineering, although still performed in other fields, e.g. mechanical engineering. Since the invention of reinforced concrete, experimental tests at Scale *II* (so called *beam busting*) have dominated the field of reinforced concrete design. Even nowadays most of the available design guidelines are based on empirical formulas obtained by fitting data from Scale *II* experimental campaigns. In some cases, e.g beam design, design procedures also require Scale *III* experimental characterization used to calibrate mathematical models at the higher scales. However, this is as far as current practice goes.

Still many questions need to be answered. What is the finest scale that we can simulate? What type of experimental data are needed? Are computational technologies already available for upscaling fine-scale concrete models? What are the needs for the future? This paper is an attempt of answering some of these questions from the point of view of the research performed within Cusatis' research group in the recent past and it does not have any velleity of being an inclusive state-of-art discussion of multiscale modeling of concrete.

2 FINE SCALE MODELS FOR CONCRETE

The formulation of a fine-scale model for concrete is the first and most important step in the

development of a multiscale computational framework. Multiscale modeling has no meaning if one does not have an accurate, calibrated and well validated fine-scale model. Paraphrasing a well known idiomatic expression used in computer science, one might say "garbage down, garbage up": if the fine-scale model to be upscaled is inaccurate and not predictive so will be the final result, regardless of the multiscale approach used.

While Scale *III* constitutive models abound in the literature—arguably there exist as many of such models as many researchers working in this field—Scale *IV* (or lower) models are scarce at best. In addition, the majority of the available fine-scale models lack generality and sufficient validation through comparison with experimental data.

The following sub-sections summarize the formulation of a Scale *III* discrete model, the Lattice Discrete Particle Model, and it's extension to account for the effect of Alkali-Silica Reaction.

2.1 *Lattice Discrete Particle Model*

The Lattice Discrete Particle Model (LDPM) formulated, calibrated, and validated by Cusatis and coworkers (Cusatis et al. 2011, Cusatis et al. 2011) simulates the mechanical interaction of coarse aggregate pieces embedded in mortar. Concrete mesostructure is constructed through the following steps. (1) The coarse aggregate pieces, whose shapes are assumed to be spherical, are introduced into the concrete volume by a try-and-reject random procedure. (2) Zero-radius aggregate pieces (nodes) are randomly distributed over the external surfaces to facilitate the application of boundary conditions. (3) A three-dimensional domain tessellation, based on the Delaunay tetrahedralization of the generated aggregate centers, creates a system of polyhedral cells (see Fig. 2) interacting through triangular facets and a lattice system composed by the line segments connecting the particle centers.

In LDPM, particle rigid body kinematics is used to describe the deformation of the lattice/particle system and the displacement jump, $[\![\mathbf{u}_C]\!]$, at the
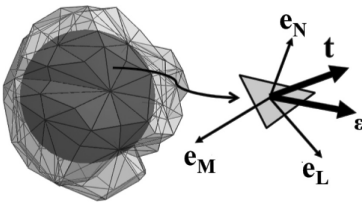

Figure 2.   LDPM cell.

centroid C of each facet is used to define measures of strain as

$$\varepsilon_\alpha = \frac{1}{r}[\![\mathbf{u}_C]\!] \cdot \mathbf{e}_\alpha \tag{1}$$

where r = interparticle distance; and $\mathbf{e}_\alpha$ with $\alpha = N, M, L$ are unit vectors defining a local system of reference attached to each facet. The displacement jump at a facet centroid shared by two adjacent particles I and J can be written as

$$[\![\mathbf{u}_C]\!] = \frac{1}{r}\left(\mathbf{U}^J + \Theta^J \times \mathbf{c}^J - \mathbf{U}^I - \Theta^I \times \mathbf{c}^I\right) \tag{2}$$

where $\mathbf{U}$ and Θ are the translational and rotational degrees of freedom of the particles and $\mathbf{c}$ is the distance from the particle center to the facet centroid. It can be shown (Cusatis and Xinwei 2013) that this definition is consistent with classical definition of strains in continuum mechanics and that, more specifically, the facet strains in Eq. 1 represent the projections of the strain tensor with reference to the facet orientation.

For given facet strains, a vectorial constitutive law governing the behavior of the material is imposed at the centroid of each facet and provides the associated tractions. In the elastic regime, the normal and shear stresses are proportional to the corresponding elastic strains: $t_N = E_N(e_N - e_N^0)$; $t_M = E_T(e_M - e_M^0)$; $t_L = E_T(e_L - e_L^0)$, where E_N = normal modulus; E_T = shear modulus; and e_N^0, e_M^0, e_L^0 are any type of stress-independent imposed strains such as, but not limited to, thermal expansion, shrinkage, and alkali-silica reaction expansion. For stresses and strains beyond the elastic limit, LDPM mesocale failure is characterized by three mechanisms: (1) cohesive fracture under tension and shear-tension; (2) compaction and pore collapse under compression; and (3) frictional behavior under compression-shear. The mathematical description of these mechanisms is reported elsewhere (Cusatis et al. 2011). Finally, the governing equations of the LDPM framework are completed through the equilibrium equations of each individual particle I

$$M_u^I \ddot{\mathbf{U}}^I - V^I \mathbf{b}^0 = \sum_{\mathcal{F}_I} A\mathbf{t}^{IJ}; \ M_\theta^I \ddot{\Theta}^I = \sum_{\mathcal{F}_I} A\mathbf{w}^{IJ} \tag{3}$$

where V^I = cell volume, M_u^I = cell mass, M_θ^I = cell rotational inertia, $\mathbf{b}^0$ = body forces, A = facet area, $\mathbf{w}^{IJ} = \mathbf{c}^I \times \mathbf{t}^{IJ}$, and $\mathbf{t}^{IJ} = t_\alpha \mathbf{e}_\alpha$.

LDPM has been calibrated and validated extensively by simulating experimental data collected at Scale *II* and *III* (Cusatis et al. 2011). In addition, LDPM was recently coupled with a Scale *V* model simulating fiber-concrete interaction (Schauffert

and Cusatis 2012) and it was adopted successfully to simulate the behavior of fiber reinforced concrete under both static (Schauffert et al. 2012) and dynamic (Smith et al. 2014) conditions.

2.2 *Simulation of alkali-silica reaction expansion*

This section deals with a Scale *IV* model (Alnaggar et al. 2013) simulating the local expansion of the gel produced by Alkali-Silica Reaction (ASR). ASR is a phenomenon affecting many structures around the world and that causes a progressive loss of load carrying capacity. In the most simple terms, ASR consist in the reaction between silica contained in the aggregate and alkali contained in the cement paste. The product of such reaction is a gel which tends to imbibe water and, consequently, to swell.The ASR model described thereinafter adopts the following assumptions: (1) Water needs to be available in the pores to act as transport medium for hydroxyl and alkali ions for ASR to occur; (2) The expansion of ASR gel is mostly due to water imbibition; (3) Continuous supply of water is needed for the swelling to continue over time; (4) The aggregate particles are assumed to have spherical shape; (5) The entire volume of each particle is assumed to be reactive; (6) Silica is smeared uniformly over each aggregate volume; and (7) the ASR chemical reaction rate is much faster than the diffusion of alkali rich water towards the reaction front.

Under these assumptions, the dissolution of silica may be assumed to progress roughly in a uniform manner in the radial direction inward from the surface towards the particle center. The gel mass, M_g, generated from an aggregate particle with diameter D, can be derived by solving a steady state radial diffusion problem governing the position of the reaction front z (Bažant and Steffens 2000). One can write

$$M_g = \kappa_a \frac{\pi D^3}{6}\left(1 - \zeta^3\right)c_s \frac{m_g}{m_s} \qquad (4)$$

where $m_g = 94.1$ g/mole, $m_s = 60.09$ g/mole are the gel and silica molar weights respectively; $\zeta = 2z/D$; c_s is the silica content; and $\kappa_a = \min\left(\langle c_a - c_a^0 \rangle/(c_a^1 - c_a^0), 1\right)$; c_a = alkali content; c_a^0 is the threshold alkali content at which, no or minimal expansion is observed; and c_a^1 is the saturation alkali content enough tocomplete the reaction of all available silica.

Furthermore, the water imbibition process can be described by relating the rate of imbibed water mass M_i to the associated thermodynamic affinity (Alnaggar et al. 2013) and a characteristic imbibition time. This leads to the following expression

$$\dot{M}_i = \frac{C_i^0}{\delta^2} e^{-\eta M_i}\left[K_i^0 \kappa_a f(T)(1 - \zeta^3)D^3 - M_i\right] \qquad (5)$$

where $f(T) = exp\left(E_{ai}/RT_0 - E_{ai}/RT\right)$; R is the universal gas constant; T is the absolute temperature in Kelvins; T_0 is a reference absolute temperature; δ is the average (or effective) distance of water transport process from the concrete around the aggregate into the ASR gel.

For given mass of imbibed water, the change in diameter of an aggregate of diameter D can be calculated from the volume variation of the ASR gel due to water imbibition as

$$\Delta D = 2\left(\frac{3M_i}{4\pi\rho_w} + \frac{D^3}{8}\right)^{1/3} - D \qquad (6)$$

This result can be then used to calculate an incompatible ASR strain, ε_N^0, to be applied to the LDPM system assuming that strain additivity holds: $\varepsilon_N^0 = (\Delta D_1/2 + \Delta D_2/2 - \delta_c)/r$; ΔD_1 and ΔD_2 are the diameter changes of the two aggregate particles sharing a generic facet. Note that the model presented herein assumes approximately that the imposed facet shear strains due to gel swelling are negligible, $\varepsilon_M^0 = \varepsilon_L^0 \approx 0$.

This model was calibrates and validated in Alnaggar et al. (2013) and it was shown to capture accurately (1) the general characteristics of ASR S-shaped expansion versus time curves; (2) the effect of stress states on observed expansion; (3) the effect of expansion on concrete strength reduction; (4) the effect of alkali content; (5) the effect of temperature; and (6) the induced crack patterns.

3 LDPM-BASED MULTISCALE METHODS

LDPM solution of Scale *I* problems is a prohibitive task even with the use of parallel computing and the most powerful computers in the world as it would require solving computational systems characterized by billions of degrees of freedom. The onlyoption to conquer such a massive computational cost is through multiscale modeling.

In general terms, multiscale modeling means seeking a certain approximated solution of a large problem by exploiting its multiscale character. Any adopted multiscale approach is meant to provide the most accurate solution for a given acceptable cost or the least computationally expensive solution for a given required accuracy. Based on this definition, a general multiscale approach that works for any situation is meaningless. Rather, multiscale approaches must be considered application and resource dependent.

3.1 *Coarse graining*

A straightforward approach to save computational cost is to formulate a coarse-grained LDPM (CG-LDPM) framework in which the particle size is fictitiously enlarged creating a particle system computationally less expensive and that only approximates the original fine system. The coarsening factor k, which characterizes the length scale change of the coarsening procedure, leads to a reduced-size coarse-grained model with $N^{CG} = N_V/k^3 + N_S/k^2$ CG-LDPM particles for N_V LDPM particles in the volume of interest and N_S particles on the associated surface.

For not excessively large value for k, one may assume that the mathematical description of the coarse-grained system is similar to the one of the original system. In this situation coarse graining can be reduced to a parameter identification problem in which the coarse-grained parameters are calibrated by fitting the original response through the coarse-grained model (Alnaggar and Cusatis 2012). The LDPM response as well as the CG-LDPM response are computed as the average response of a statistically significant number of particle realizations—typically at least three.

For a generic test setup i and for a set of CG-LDPM parameters $\mathbf{x}$ the error between the CG-LDPM response and the reference LDPM average response is

$$\mathbf{R}_i(\mathbf{x}) = \frac{1}{\max(\overline{\mathbf{F}}_i)}\left(\frac{1}{N}\sum_{j=1}^{N}\mathbf{C}_i^j(\mathbf{x}) - \overline{\mathbf{F}}_i\right) \quad (7)$$

The vector $\overline{\mathbf{F}}_i$ is a discrete sampling of a characteristic load vs. deformation curve relevant to the average LDPM response; $\mathbf{C}_i^j(\mathbf{x})$ is the sampled response for a given CG-LDPM specimen j; and N = number of different particle realizations of the CG specimen. The overall error across all different test setups can be then computed as $\mathbf{E}(\mathbf{x}) = \sum_{i=1}^{n}\mathbf{R}_i(\mathbf{x})$ (n = number of different test setups) and its minimization leads to the optimal CG-LDPM parameter set.

One key aspect of the coarse graining procedure used in this study is the selection of the different test setups used to compute the error $\mathbf{E}(\mathbf{x})$. The minimum number of test setups needed for the identification of all CG-LDPM parameters are: (1) hydrostatic compression tests; (2) unconfined compression tests; (3) fracture tests; and (4) confined compression tests relevant to at least two confinement pressures (low and high).

Of course a different number of test setups can be also used if only a subset of all parameters need to be identified. For example, if the coarse-grained model is sought for an application for which the

triaxial compressive behavior is unimportant, then the CG parameters can be identified by using simply fracture tests and unconfined compression tests.

Figures 3a through e show an example of coarse graining procedure used to obtain a CG-LDPM model with a coarsening factor $k = 3$ and to be used for the simulation of the combined bending and shear failure of a reinforced concrete shear wall. The main LDPM parameters relevant for this problem are: meso-scale tensile strength σ_t, tensile characteristic length l_t, softening exponent n_t, shear to tension strength ratio σ_s/σ_t and initial friction μ_0. The tests required to identify these parameters are a fracture test and an unconfined compression test. For the fracture test, the 3 point bending test is used and the test setup is shown in Figure 3a, featuring a 1130 mm span notched beam with 100×200 mm cross-section and 100 mm notch. To reduce the computational cost, only the notched central part is simulated by LDPM/CG-LDPM elements while the remaining parts are simulated with elastic solid finite elements. 3 different particle realizations were generated for both models. The response average of the LDPM model beams was computed first ($\overline{\mathbf{F}}_1$); then, using a automatic parameter identification algorithm, for each parameter set at each iteration, the response average for CG-LDPM model beams was computed ($\overline{\mathbf{C}}_i(\mathbf{x})$) and used in Eq. 7 to calculate the error vector for the 3PBT $\mathbf{R}_1(\mathbf{x})$. At the same iteration, the error vector of the unconfined compression testwas also computed ($\mathbf{R}_2(\mathbf{x})$). The unconfined compression test setup is shown in Figure 3c, where the simulation of a cylinder of 150 mm diameter and 300 mm height is performed using 3 LDPM and 3 CG-LDPM different particle realizations. The LDPM response average of the UCC test ($\overline{\mathbf{F}}_2$) along with the CG-LDPM response average ($\overline{\mathbf{C}}_i(\mathbf{x})$) for the iteration were used to calculate $\mathbf{R}_2(\mathbf{x})$. A typical load displacement response for both models in 3PBT at one of the iterations is shown in Figure 3b along with their difference used in calculating the error. Similarly, for the UCC test, a typical response for both models is shown in Figure 3d at the same iteration. With these data, the procedure calculates the overall normalized error for all tests by combining the discrete error vectors of the two tests. For the effect of all tests to be equally weighted, the sizes of all test error vectors are all fixed at the same value ℓ_i, which was here set to 1000 points. The overall error vector $\mathbf{E}(\mathbf{x})$ for the test results shown in Figure 3b and d is shown in Figure 3e. This overall error vector is used by the identification procedure to advance to the next iteration where the procedure updates the values of the aforementioned 5 parameters and runs again another group of simulations for the
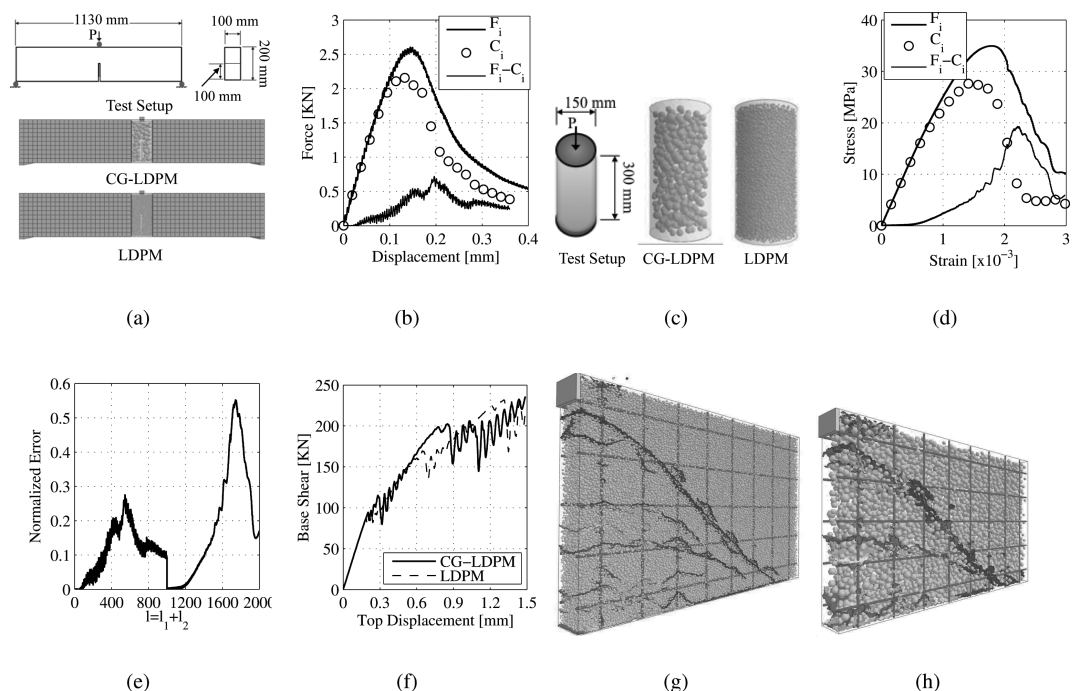
27

Figure 3. (a) Three-point bending test setup. (b) Three-point bending test responses. (c) Unconfined compression test setup. (d) Unconfined compression response. (e) Combined error. (f) Shear wall response. (g) LDPM crack pattern. (h) CG-LDPM crack pattern.

CG-LDPM model test. The iterations keep running until the sum of the squares of $\mathbf{E}(\mathbf{x})$ is less than a predefined tolerance (usually 0.001). After calibration, the identified parameters can be used along with the coarsening factor to generate and simulate CG-LDPM models for the problem of interest.

The simulation of RC shear walls is used here to show the validity and effectiveness of CG-LDPM. Reinforced concrete walls are used in buildings for various reasons but mainly to carry lateral horizontal loads from earthquake or wind. A small reinforced concrete shear wall is modeled here using a coarsening factor $k = 3$ and utilizing the identified parameters of the aforementioned identification. The wall dimensions are 1 m × 0.6 m × 0.10 m with 2 rebar meshes spaced at 120 mm with cross sectional area of 37.5 mm². A lateral displacement is applied in-plane at one side of the wall using a rigid loading plate of 6 cm height and 10 cm width. The total base shear versus plate displacement is shown in Figure 3f. Generally, the CG-LDPM response agrees very well with LDPM response. It exactly matches the LDPM response in the elastic regime, then as cracking initiates, the CG-LDPM response still remains in very good agreement

with the reference LDPM average response. The CG-LDPM load versus displacement curve contains all the features of the reference curve, including the two drops in load carrying capacities corresponding to the initiation and propagation of the two main cracks visible at failure. Crack pattern distributions for both LDPM and CG-LDPM models are shown in Figure 3g and h, respectively. CG-LDPM captures well the crack distributions, locations and patterns but as a lumped version of the smeared cracks in the LDPM case. By comparing both crack patterns within the reinforcement panels, each major CG-LDPM crack corresponds to 2 or 3 major cracks in the LDPM wall.

The ratio between the DOFs of the LDPM model to the CG-LDPM model is 963846/56532 = 17. With this ratio, the total simulation cost for LDPM and CG-LDPM are 640 SU's to 24 SU's where, the SU stands for a computational Service Unit defined as using 1 processor for 1 hour. So, with a coarsening factor of $k = 3$, the computational cost of CG-LDPM model is about 1/26.7 times the original LDPM model. While the reduction of computational cost is expected to be within the same order of reduction in degrees of freedom (i.e. about 17 times), another factor adds to the

28

computational cost for the fine model in case of using multi-processor computing systems (MPI). In these systems, the computational domain is distributed among a group of processors that do not necessarily even contained by the same node, each processor advances the solution of that part of the domain for one time step, then they communicate to transfer their information at the boundaries. Such communication is a function of the number of processors, number of nodes involved and data transfer speed. So, for the shear wall case, the CG-LDPM model used only 2 nodes with 8 processors each, while to run the LDPM model for the shear wall, 8 nodes with 8 processors each were needed. This explains the reason for additional simulation time for the fine model that boosted the reduction of computational cost from the expected value of 17 up to about 27.

3.2 *Bridging Scale Method*

The basic idea of Briding Scale Method (BSM) (Wagner and Liu 2003) is to decompose the entire physical domain into two separate models, namely the fine-scale model, only present in a limited portion of the entire domain, and the coarse-scale model present everywhere in the domain. The coarse-scale model aims at representing the average response of the entire domain, while the fine-scale model captures fine features of the response which cannot be resolved by the coarse-scale model. In this section a BSM scheme is presented in which the fine-scale model is LDPM.

In the limited zone in which the fine-scale and the coarse-scale models coexist the response can be expressed as

$$\mathbf{q} = \bar{\mathbf{q}} + \mathbf{q}' \qquad (8)$$

where the fine-scale solution, $\mathbf{q}$, is decomposed in its average response, $\bar{\mathbf{q}}$, and the fine-scale correction, $\mathbf{q}'$. The basic idea of BSM is to describe the average response through interpolation of the coarse-scale solution $\bar{\mathbf{q}} = \mathbf{NQ}$, where $\mathbf{N}$ is the shape function matrix calculated at the fine scale nodes and the vector $\mathbf{Q}$ collects the coarse-scale degrees of freedom.

The fine-scale equations of motion can be written as

$$\mathbf{m}\ddot{\mathbf{q}} = \mathbf{r} \qquad (9)$$

where $\mathbf{r} = \mathbf{f}_{ext} - \mathbf{f}_{int}$ is the imbalance between external and internal forces. By substituting Eq. 8 into Eq. 9 one can write $\mathbf{mN}\ddot{\mathbf{Q}} = \mathbf{r} - \mathbf{m}\ddot{\mathbf{q}}'$, which, premultiplied by the transpose of $\mathbf{N}$, leads to

$$\mathbf{N}^T\mathbf{m}\mathbf{N}\ddot{\mathbf{Q}} = \mathbf{N}^T\mathbf{r}(\mathbf{q}) - \mathbf{N}^T\mathbf{m}\ddot{\mathbf{q}}' \qquad (10)$$

Furthermore, by imposing $\bar{\mathbf{q}}$ to be the mass-weighted average of $\mathbf{q}$ one can write (Wagner and Liu 2003) $\bar{\mathbf{q}} \approx \mathbf{Pq}$ where $\mathbf{P} = \mathbf{NM}^{-1}\mathbf{N}^T\mathbf{m}$, $\mathbf{M} = \mathbf{N}^T\mathbf{mN}$; and $\mathbf{q}' \approx \mathbf{Sq}$ where $\mathbf{S} = \mathbf{I} - \mathbf{P}$, and, finally,

$$\mathbf{M}\ddot{\mathbf{Q}} = \mathbf{R}(\mathbf{q}) \qquad (11)$$

Equation 11 represents the equation of motion of the coarse-scale (in the zone overlapped with the fine-scale) and it was obtained by setting $\mathbf{R} = \mathbf{N}^T\mathbf{r}(\mathbf{q})$ and by using the identity $\mathbf{N}^T\mathbf{mS} \equiv 0$.

Since the fine-scale domain covers only a small portion of the entire domain, boundary conditions at the coarse-fine interface need to be formulated in such a way information across the scales is transferred correctly without spurious effects, such as high frequency wave reflections.

Non-Reflecting Boundary Condition (NRBC) are typically formulated by adding a layer of elements accompanied by a layer of nodes (ghost nodes) outside of the fine scale domain. The ghost nodes account for the removed domain in the fine scale, namely the movement of the ghost nodes is prescribed such that the remaining fine-scale nodes behave as if the fine scale existed everywhere.

One way to formulate the non-reflecting boundary condition is to assume that the mesh structure of the fine scale is periodic (Wagner et al. 2004). However, the particles constructing LDPM mesh are generated randomly, which means that the mesh does not have a periodic structure. To solve this problem, the so-called Periodic Transition Zone (PTZ) is introduced outside the LDPM mesh, see Figure 4a. The elements in the PTZ have a similar size to the LDPM mesh, in order to ensure a smooth transition from LDPM to PTZ; then, the non-reflecting boundary condition is formulated based on the PTZ. The kinematic constraint between LDPM and PTZ can be enforced by the commonly used master-slave approach.

Here we discuss how to construct such transition zone based on linear tetrahedral element and formulate the non-reflecting boundary condition for it. To ensure periodicity, the PTZ is composed of repeated unit cells. Each unit cell is a cube, which can be further divided into five linear tetrahedral elements, see Figure 4(b) and (c). The stiffness matrix of the unit cell is obtained by assembling the element stiffness matrix of each individual tetrahedron $\mathbf{K}_i^t$ ($i = 1, \ldots, 5$).

$$\mathbf{K} = \sum_{i=1}^{5} \mathbf{K}_i^t = \begin{bmatrix} \mathbf{k}_{11} & \mathbf{k}_{12} & \cdots & \mathbf{k}_{18} \\ \mathbf{k}_{21} & \mathbf{k}_{22} & \cdots & \mathbf{k}_{18} \\ \vdots & \vdots & \ddots & \vdots \\ \mathbf{k}_{81} & \mathbf{k}_{82} & \cdots & \mathbf{k}_{88} \end{bmatrix}. \qquad (12)$$
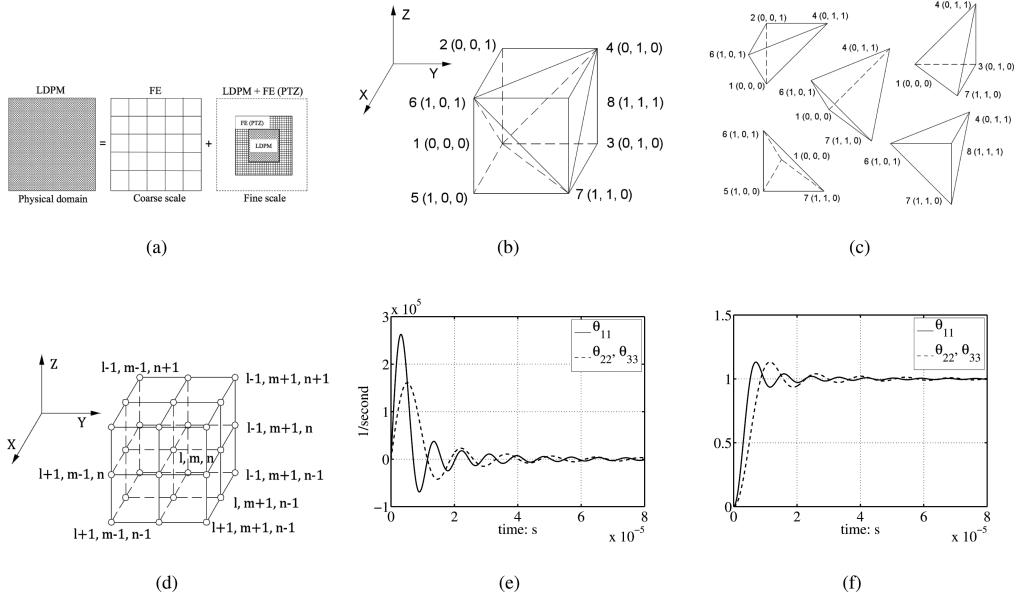
Figure 4.   (a) Domain decomposition. (b) Unit cell in PTZ. (c) Decomposition of unit cell. (d) Unit cell numbering. (e) Time history kernel $\theta(t)$. (f) Integration of time history kernel $\int \theta(t)\mathrm{d}t$.

Here $\mathbf{k}_{ij}$ is a matrix of size 3×3 and has the physical meaning of the applied force on node i caused by the displacement of node j, where i,j are local numbers defined in a unit cell; due to the symmetry of $\mathbf{K}$, one has $\mathbf{k}_{ij} = \mathbf{k}_{ji}^{\mathrm{T}}$.

Let us denote a generic node by a triad (l, m, n), where l, m, n are integers going from negative infinity to positive infinity. Its neighboring nodes are indexed as showed in Figure 4(d). For brevity, $\mathbf{u}_{l-1,m-1,n-1}$ is denoted by $\mathbf{q}_{-1,-1,-1}$, where the subscripts are their index triad subtracted by (l, m, n), etc. Then, one can find the following coefficients: $\mathbf{K}_{0,0,0} = \sum_{i=1}^{8} \mathbf{k}_{ii}$, $\mathbf{K}_{1,0,0} = \mathbf{K}^{\mathrm{T}}_{-1,0,0} = \mathbf{k}_{15} + \mathbf{k}_{26} + \mathbf{k}_{37} + \mathbf{k}_{48}$, $\mathbf{K}_{1,0,0} = \mathbf{K}^{\mathrm{T}}_{-1,0,0} = \mathbf{k}_{15} + \mathbf{k}_{26} + \mathbf{k}_{37} + \mathbf{k}_{48}$, $\mathbf{K}_{0,1,0} = \mathbf{K}^{\mathrm{T}}_{0,-1,0} = \mathbf{k}_{13} + \mathbf{k}_{24} + \mathbf{k}_{57} + \mathbf{k}_{68}$, $\mathbf{K}_{0,0,1} = \mathbf{K}^{\mathrm{T}}_{0,0,-1} = \mathbf{k}_{12} + \mathbf{k}_{34} + \mathbf{k}_{56} + \mathbf{k}_{78}$, $\mathbf{K}_{1,1,0} = \mathbf{K}^{\mathrm{T}}_{-1,-1,0} = \mathbf{k}_{17}$, $\mathbf{K}_{0,1,1} = \mathbf{K}^{\mathrm{T}}_{0,-1,-1} = \mathbf{k}_{14}$, $\mathbf{K}_{1,0,1} = \mathbf{K}^{\mathrm{T}}_{-1,0,-1} = \mathbf{k}_{16}$, $\mathbf{K}_{1,-1,0} = \mathbf{K}^{\mathrm{T}}_{-1,1,0} = \mathbf{k}_{46}$, $\mathbf{K}_{0,1,-1} = \mathbf{K}^{\mathrm{T}}_{0,-1,1} = \mathbf{k}_{67}$, $\mathbf{K}_{1,0,-1} = \mathbf{K}^{\mathrm{T}}_{-1,0,1} = \mathbf{k}_{47}$.

In absence of external foce, for node (l, m, n), the equation of motion reads $\mathbf{m}\ddot{\mathbf{q}}_{lmn} = -\mathbf{f}_{lmn}^{int}$ which can be rewritten as

$$\ddot{\mathbf{q}}_{lmn} = \sum_{l'=l^-}^{l^+} \sum_{m'=m^-}^{m^+} \sum_{n'=n^-}^{n^+} \mathbf{H}_{l-l',m-m',n-n'}\mathbf{q}_{l',m',n'} \qquad (13)$$

where $\mathbf{H} = -\mathbf{M}^{-1}\mathbf{K}$, $l^- = l-1$, $l^+ = l+1$, etcetera. Applying similar procedures discussed in Farrell et al. (2007) and Wagner et al. (2004) to Eq. 13, the non-reflecting boundary condition is given as a displacement conditon for the ghost nodes

$$\mathbf{q}_{1mn}(t) = \sum_{m'=M^-}^{M^+} \sum_{n'=N^-}^{N^+} \int_0^t \theta_{o'p'}(\xi)\mathbf{q}_{0m'n'}(\tau)\mathrm{d}\tau \qquad (14)$$

where $\xi = t - \tau$, $o' = m - m'$, $p' = n - n'$, $M^- = -M/2+1$, $M^+ = M/2$, $N^- = -N/2+1$, $N^+ = N/2$ and M, N are the number of unit cells in Y and Z direction, respectively, $\theta_{m,n}(t)$ is the so-called time history kernel corresponding to boundry node located at $(0, m, n)$.

If there are only translational DOFs per node, e.g. linear tetrahedral element, θ is size of 3×3. For a PTZ structure where cube size = 0.01 m, Young's modulus = 30000 MPa, Possion ratio = 0.2, material density = 2500 kg/m^3. The diagonal components of θ are plotted in Figure 4e and f, while the off-diagonal compnents are basically negilible.

To illustrate the effectiveness of BSM, the wave propagation in a 3D elastic bar is studied, see Figure 5. The material parameters of this bar are: Young's modulus = 3×10^{10} Pa, density = 2500 kg/m^3, Poisson's ratio = 0.2. A displacement excitation $D(t)$ is applied on the left end. Its profile is defined by $D(t) = A_1 \sin(\pi t/T) + A_2 \sin(30\pi t/T)$ for $t \leq T$ and $D(t) = 0$ otherwise, which consists of both high frequency and low frequency sinusoidal waves, see Figure 6a. $A_1 = 0.1$ m and $A_2 = 0.01$ m are the amplitudes of the low frequency wave and the high frequency wave, respectively. $T = 1 \times 10^{-3}$ sec is half the period of the low frequency wave.
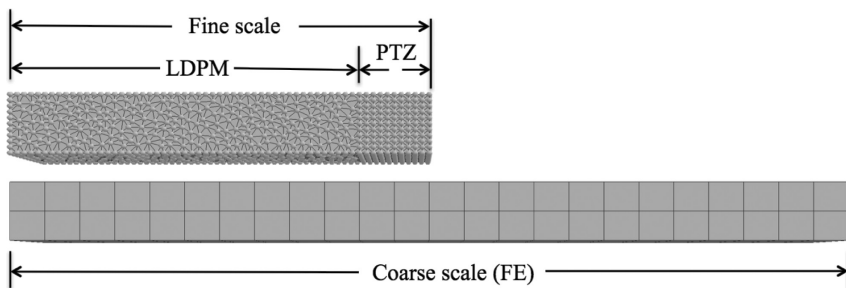
Figure 5. BSM domain decomposition of 3D bar.
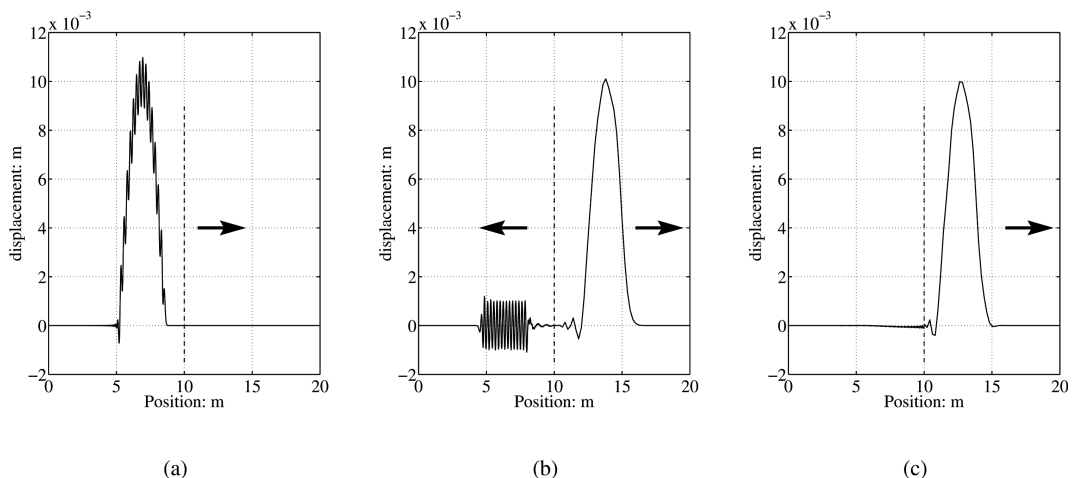

(a) (b) (c)

Figure 6. (a) Wave impulse. (b) Reflection of high frequency wave. (c) Solution with high frequency energy dissipation.

Figure 6b show the response without NRBC. As expected, the high frequency signal that is not supported by the coarse mesh is reflected at the fine-coarse interface. On the contrary, as shown in Figure 6c, such reflection is avoided by using the NRBC. As the impulse passes the interface, the high frequency component is removed by the non-reflecting boundary condition while the low frequency component is carried on by the coarse scale.

3.3 Mathematical homogenization

Another multiscale approach able to upscale LDPM to Scale *II* and *III* and eventually to Scale *I* by using continuum based theories and computational methods, is the so-called mathematical homogenization. Mathematical homogenization was first introduced by Babuska (1975) and then used by many other authors (Hassani and

Hinton 1998, Fish and Wagiman. 1993) to obtain homogenized constitutive equations starting from fine-scale models. Most of the adopted fine-scale models, however, were formulated within classical continuum mechanics. Recently Fish et al. (2007) introduced the Generalized Mathematical Homogenization (GMH) for the multiscale analysis of atomistic periodic systems. In this section, this theory is further developed for the two-scale homogenization of LDPM. The main difference compared to previous work is that the proposed formulation also accounts for the rotational equilibrium equation of the particles.

3.3.1 Formulation

In order to perform a two-scale asymptotic homogenization, a periodic discrete system, composed by a number of adjacent RVEs (or Unit Cells), is considered. Two separate length scales and the corresponding coordinate systems, **x** and **y**, are

31

introduced to represent the macroscopic domain, in which the problem is defined as continuous with no detail of material heterogeneity, and the meso-scale domain, in which heterogeneity is modeled by LDPM. If the separation of scales exists, one can write the following relationship linking macro and meso coordinate systems

$$\mathbf{x} = \eta \mathbf{y} \qquad 0 < \eta << 1 \qquad (15)$$

where η is a very small positive scalar. In addition, the displacement of a generic particle P_I, $\mathbf{U}^I = \mathbf{u}(\mathbf{x}^I, \mathbf{y}^I)$, can be approximated by means of the following asymptotic expansion

$$\mathbf{u} \approx \mathbf{u}^0 + \eta \mathbf{u}^1 \qquad (16)$$

where only terms up to order $\mathcal{O}(\eta)$ are considered. Functions $\mathbf{u}^0(\mathbf{x},\mathbf{y})$, and $\mathbf{u}^1(\mathbf{x},\mathbf{y})$ are continuous with respect to $\mathbf{x}$ and discrete (i.e. defined only at finite number of points) with respect to $\mathbf{y}$.

In order to define the asymptotic expansion for rotations, it is convenient first to postulate the existence of a continuous displacement-like field $d^\eta(\mathbf{x})$ such that $2\Theta^I = \nabla \times d^\eta|_{\mathbf{x}=\mathbf{x}^I}$. If then $d^\eta(\mathbf{x})$ is replaced by a two-scale approximation similar to the one in Eq. 16, one can write, $\Theta^I = \theta(\mathbf{x}^I, \mathbf{y}^I)$, and

$$\theta \approx \eta^{-1}\omega^0 + \varphi^0 + \omega^1 + \eta \varphi^1 \qquad (17)$$

where $2\omega^0 = \nabla_y \times d^0$; $2\varphi^0 = \nabla_x \times d^0$; $2\omega^1 = \nabla_y \times d^1$; $2\varphi^1 = \nabla_x \times d^1$; and subscripts x and y identify the nabla operator in the coarse and fine scale, respectively. Thus, ω^0, ω^1 should be interpreted as rotations in the fine scale whereas φ^0, φ^1 as the corresponding coarse scale rotations. It is worth observing here that, contrarily to the expansion of displacements, the asymptotic expansion for rotations features a term of order $\mathcal{O}(\eta^{-1})$ and two distinct terms of order $\mathcal{O}(1)$.

In the macroscopic coordinate $\mathbf{x}$, the difference in position between node P_I and P_J can be considered as infinitesimal. Hence, in order to obtain the asymptotic expansion of strains, it is convenient first to obtain the Taylor series expansion of displacement and rotation at nodes P_J around point P_I of coordinate $\mathbf{x}^I = \mathbf{X}$ in x-coordinate system. By assuming that the displacement and rotation fields in Eqs. 16 and 17, are continuous and differentiable with respect to $\mathbf{x}$, one can write

$$u_i(\mathbf{x}^J, \mathbf{y}^J) = u_i^J + u_{i,j}^J x_j^{IJ} + \frac{1}{2} u_{i,jk}^J x_j^{IJ} x_k^{IJ} + \cdots \quad (18)$$

$$\theta_i(\mathbf{x}^J, \mathbf{y}^J) = \theta_i^J + \theta_{i,j}^J x_j^{IJ} + \frac{1}{2} \theta_{i,jk}^J x_j^{IJ} x_k^{IJ} + \cdots \quad (19)$$

where $u_i^J = u_i(\mathbf{X}, \mathbf{y}^J)$; $u_{i,j}^J = \partial u_i / \partial x_j(\mathbf{X}, \mathbf{y}^J)$; $u_{i,jk}^J = \partial^2 u_i / \partial x_j \partial x_k(\mathbf{X}, \mathbf{y}^J)$; $\theta_i^J = \theta_i(\mathbf{X}, \mathbf{y}^J)$; $\theta_{i,j}^J = \partial \theta_i / \partial x_j(\mathbf{X}, \mathbf{y}^J)$; $\theta_{i,jk}^J = \partial^2 \theta_i / \partial x_j \partial x_k(\mathbf{X}, \mathbf{y}^J)$; x_j^{IJ} is a vector connecting node P_I to node P_J in the $\mathbf{x}$ space. By substituting Eqs. 16 and 17 into Eq. 1, and using the Taylor expansion of displacement and rotation of node P_J around node P_I (Eqs. 18 and 19) one obtains the multiple scale definition of facet strain in the following form

$$\varepsilon_\alpha = \eta^{-1}\varepsilon_\alpha^{-1} + \varepsilon_\alpha^0 + \eta \varepsilon_\alpha^1 \qquad (20)$$

where $\alpha = N, M, L$.

It is worth noting that in this section as well as in the rest of the paper the superscript IJ is dropped when the permutation of I and J is not associated to a sign change.

In order to obtain the correct scale separation of the governing equations, a rescaling of the discrete equilibrium equations needs to be performed. This is pursued by assuming that the material density, mass per unit volume, is of order zero: $\rho \sim \mathcal{O}(1)$, which along with the displacement asymptotic expansion implies that the left-hand-side of the first equation in Eq. 3 is $\sim \mathcal{O}(\eta^3)$. By dividing both sides of the first equation in Eq. 3 by η^3, and considering that all length variables should be considered $\sim \mathcal{O}(\eta^1)$, one obtains

$$\bar{M}_u^I \ddot{\mathbf{u}}^I - \bar{V}^I \mathbf{b}^0 = \eta^{-1} \sum_{\mathcal{F}_I} \bar{A} t_\alpha \mathbf{e}_\alpha^{IJ} \qquad (21)$$

where $\bar{M}_u^I = M_u^I / \eta^3$, $\bar{V}^I = V^I / \eta^3$, $\bar{A} = A / \eta^2$ are all quantities $\sim \mathcal{O}(1)$. For reason of dimensionality, body forces b_i^0 can be always assumed to be proportional to gravity ρg and, consequently, they can be considered $\mathcal{O}(1)$ quantities as well.

One can rescale the rotational equation in a similar fashion by recognizing that, according to the previous discussion, the rotational moment of inertia is $\sim \mathcal{O}(\eta^5)$. Dividing both sides of the second equation in Eq. 3 by η^4 one obtains

$$\eta \bar{M}_\theta^I \boldsymbol{\theta}^I = \eta^{-1} \sum_{\mathcal{F}_I} \bar{A} \eta^{-1} w_\alpha \mathbf{e}_\alpha^{IJ} \qquad (22)$$

where $\bar{M}_\theta^I = M_\theta^I / \eta^5$ is $\sim \mathcal{O}(1)$.

In the elastic regime one can write: $t_\alpha = \eta^{-1} t_\alpha^{-1} + t_\alpha^0 + \eta^1 t_\alpha^1$, where E^α is assumed to be $\sim \mathcal{O}(1)$; $t_\alpha^{(\cdot)} = E^\alpha \varepsilon_\alpha^{(\cdot)}$, and $p_\alpha = \eta^{-1} w_\alpha = \eta^{-1} p_\alpha^{-1} + p_\alpha^0 + \eta^1 p_\alpha^1$ where $p_\alpha^{(\cdot)} = \bar{c}^I \times t_\alpha^{(\cdot)}$. Introducing these traction expressions into the rescaled equilibrium equations leads to

$$\eta^{-2} \sum_{\mathcal{F}_I} \bar{A} t_\alpha^{-1} \mathbf{e}_\alpha^{IJ} + \eta^{-1} \sum_{\mathcal{F}_I} \bar{A} t_\alpha^0 \mathbf{e}_\alpha^{IJ} + \sum_{\mathcal{F}_I} \bar{A} t_\alpha^1 \mathbf{e}_\alpha^{IJ}$$
$$- \bar{M}_u^I \ddot{\mathbf{u}}^{0I} + \bar{V}^I \mathbf{b}^0 + \mathcal{O}(\eta) = \mathbf{0} \qquad (23)$$

and

$$\eta^{-2} \sum_{\mathcal{F}_I} \overline{A}\, p_\alpha^{-1} \mathbf{e}_\alpha^{IJ} + \eta^{-1} \sum_{\mathcal{F}_I} \overline{A}\, p_\alpha^0 \mathbf{e}_\alpha^{IJ} - \overline{M}_\theta^I \ddot{\omega}^{0I}$$
$$+ \sum_{\mathcal{F}_I} \overline{A}\, p_\alpha^1 \mathbf{e}_\alpha^{IJ} + \mathcal{O}(\eta) = \mathbf{0} \qquad (24)$$

in which terms of different orders are gathered together.

Let's first consider the equilibrium equations at the $\mathcal{O}(\eta^{-2})$ scale. From Eqs. 23 and 24, it is evident that the $\mathcal{O}(\eta^{-2})$ equilibrium equations represent the equilibrium of all particles in the RVE subject to the stress tractions t_α^{-1} and the moment tractions q_α^{-1} and without any applied external load. Consequently, solution of the $\mathcal{O}(\eta^{-2})$ problem implies $t_\alpha^{-1} = 0$ and $q_\alpha^{-1} = 0$, which in turn, leads to $\varepsilon_\alpha^{-1} = 0$. This can be expressed as rigid body rotation and translation of the RVE

$$u_i^0(\mathbf{x}, \mathbf{y}) = v_i^0(\mathbf{x}) + \varepsilon_{ijk} y_k \omega_j^0(\mathbf{x}) \qquad (25)$$

in which the fields $\mathbf{v}^0$ and ω^0 are only dependent on $\mathbf{x}$, i.e. they do not change within the unit cell, and they can be calculated when kinematic boundary conditions are specified for the $\mathcal{O}(\eta^{-2})$ problem. These boundary conditions must describe the physical fact that the RVE is attached to a point in the macroscopic continuum. Hence, $\mathbf{v}^0$ must correspond to the macroscopic displacement field and ω^0 must be equal to the macroscopic rotation field: $\varphi^0 = \omega^0$. Since ω^0 is constant over the RVE, then φ^0 is also constant in the RVE.

On the basis of Eq. 25 and the discussion above, one can rewrite the $\mathcal{O}(1)$ strains as

$$\varepsilon_\alpha^0 = \overline{r}^{-1} \left[\!\left[u_{Ci}^1 \right]\!\right] e_{\alpha i}^{IJ} + P_{ij}^\alpha \left(\gamma_{ij} + \varepsilon_{jmn} \kappa_{im} y_n^c \right) \qquad (26)$$

where $\gamma_{ij} = v_{j,i}^0 - \varepsilon_{ijk} \omega_k^0$ and $\kappa_{ij} = \omega_{j,i}^0$ are the macroscopic Cosserat strain and curvature tensors, respectively. $\mathbf{y}^c$ is the position vector of the centroid of the common facet between particle I and J and $P_{ij}^\alpha = n_i^{IJ} e_{\alpha j}^{IJ}$ is a projection operator.

Strains of order $\mathcal{O}(\eta)$ can also be rewritten by taking into account Eq. 25. One gets

$$\varepsilon_\alpha^1 = (u_{i,j}^{1J} y_j^{IJ} + \varepsilon_{ijk} \varphi_j^{1J} \overline{c}_k^J + \varepsilon_{ijk} \omega_{j,m}^{1J} y_m^{IJ} \overline{c}_k^J$$
$$- \varepsilon_{ijk} \varphi_j^{1I} \overline{c}_k^I + v_{i,jk}^0 y_j^{IJ} y_k^{IJ}/2$$
$$+ \varepsilon_{ijk} \omega_{j,mn}^0 y_m^{IJ} y_n^{IJ} y_k^c/2 + \varepsilon_{ijk} \omega_{j,m}^0 y_m^{IJ} \overline{c}_k^J) e_{\alpha i}^{IJ}/\overline{r} \qquad (27)$$

Although rigorously demonstrated only in the linear elastic case, the result discussed above can be assumed to hold also for a general nonlinear case. In this more general situation, the $\mathcal{O}(\eta^{-1})$ component of the asymptotic expansion of strain are assumed to be zero a priori. Therefore, tractions t_α^{IJ} are functions of $\varepsilon_\alpha^0 + \eta \varepsilon_\alpha^1$ and they can be expanded in Taylor series around the $\mathcal{O}(1)$ component of strain. In this way, the multiple scale equilibrium equations in Eqs. 23, and 24 are still valid if one sets $t_\alpha^0 = t_\alpha(\varepsilon_N^0, \varepsilon_M^0, \varepsilon_L^0)$, $w_\alpha^0 = w_\alpha(\varepsilon_N^0, \varepsilon_M^0, \varepsilon_L^0)$, $t_\alpha^1 = (\partial t_\alpha/\partial \varepsilon_\beta^0) \varepsilon_\beta^1$, and $w_\alpha^1 = (\partial w_\alpha/\partial \varepsilon_\beta^0) \varepsilon_\beta^1$.

The unit cell problem is governed by the $\mathcal{O}(\eta^{-1})$ terms in Eqs. 23 and 24. Considering those terms and scaling back all the variables, one can write

$$\sum_{\mathcal{F}_I} A t_\alpha^0 \mathbf{e}_\alpha^{IJ} = 0; \quad \sum_{\mathcal{F}_I} A (t_\alpha^0 \mathbf{c}^I \times \mathbf{e}_\alpha^{IJ}) = 0 \qquad (28)$$

Eqs. 28 are the force and the moment equilibrium equations of each single particle inside the unit cell subjected to $\mathcal{O}(1)$ facet traction t_α^0. One should consider the fact that t_α^0 is function of ε_α^0, which consist of a coarse and a fine scale term (see Eqs. 26). Therefore, Eq. 28 states that macroscopic strain $\gamma_{ij} = v_{j,i}^0 - \varepsilon_{ijk} \omega_k^0$ and curvature $\kappa_{ij} = \omega_{j,i}^0$ tensors should be applied on the unit cell and the fine scale quantities u^1 and ω^1 must be calculated in a way that preserve equilibrium of each particle inside the unit cell. In other words, applying appropriate boundary condition on the boundary of the unit cell along with projecting macroscopic kinematic tensors on all unit cell facets, one can calculate the fine scale solution by solving equilibrium Eqs. 28 for all particles.

Finally, let us consider the $\mathcal{O}(1)$ equilibrium equations in Eqs. 23 and 24. The $\mathcal{O}(1)$ translation equilibrium equation for each particle in the unit cell, reads

$$M_u^I \ddot{u}_i^{0I} = \eta \sum_{F_I} A \frac{\partial t_i^{IJ}}{\partial \varepsilon_\alpha^0} \varepsilon_\alpha^1 + V^I b_i^0 \qquad (29)$$

where all the variables have been scaled back in the original system of reference, and $t_i^{IJ} = t_\beta e_{\beta i}^{IJ}$. By using Eq. 25 and by averaging the contribution of all particles in the unit cell, one can write

$$\rho_u \ddot{v}_i^0 = \frac{1}{V_0} \sum_I \sum_{F_I} \eta A \frac{\partial t_i^{IJ}}{\partial \varepsilon_\alpha^0} \varepsilon_\alpha^1 + b_i \qquad (30)$$

where V_0 is the volume of the unit cell; $\rho_u = \sum_I M_u^I/V_0$ is the mass density of the macroscopic continuum. It can be shown that, after some algebraic manipulations, Eq. 29 can be rewritten as

$$\rho_u \ddot{v}_i^0 = \frac{1}{2V_0} \sum_I \sum_{\mathcal{F}_I} A r \frac{\partial t_i^{IJ}}{\partial x_j} n_j^{IJ} + b_i \qquad (31)$$

33

Finally, by considering identity equation (1)
$\partial(t_i^{IJ} n_j^{IJ})/\partial x_j = \partial t_i^{IJ}/\partial x_j n_j^{IJ} + t_i^{IJ} \partial n_j^{IJ}/\partial x_j$ and (2)
$\partial n_j^{IJ}/\partial x_j = 0$ for the periodicity of the problem; and by recalling that $t_i^{IJ} = t_\alpha e_{\alpha i}^{IJ}$, one obtains

$$\rho_u \ddot{v}_i^0 = \frac{\partial \sigma_{ji}^0}{\partial x_j} + b_i \tag{32}$$

and

$$\sigma_{ij}^0 = \frac{1}{2V_0} \sum_I \sum_{\mathcal{F}_I} A r t_\alpha^0 P_{ij}^\alpha \tag{33}$$

Equation 32 is the classical partial differential equation governing the equilibrium of continua whereas Eq. 33 provides the macroscopic stress tensor by averaging the solution of the unit cell problem.

The $\mathcal{O}(1)$ moment equilibrium equation is considered next. Since the purpose in this section is to average the equation of motion of all particles inside the unit cell, to have consistent formulation for all particles, one should consider moment of all forces with respect to a fixed point in space. For the generic particle I, by taking the moment about the mass centroid of the unit cell (point O) and by considering the results of the $\mathcal{O}(\eta^{-2})$ problem, one can write

$$M_u^I \varepsilon_{ijk} x_j^I \left(\ddot{v}_k^0 + \varepsilon_{kmn} \eta^{-1} \ddot{\omega}_m^0 x_n^I \right) + \eta^{-1} M_\theta^I \ddot{\omega}_i^0$$
$$= \eta \sum_{\mathcal{F}_I} A \frac{\partial w_i^{IJ}}{\partial \varepsilon_\alpha^0} \varepsilon_\alpha^1 + V^I \varepsilon_{ijk} x_j^I b_k^0 \tag{34}$$

where $w_i^{IJ} = \varepsilon_{ijk} x_j^C t_k^{IJ}$ is the moment of facet traction with respect to the unit cell center. x_j^I and x_j^C are the position vectors of particle I and contact point C, respectively, in a system of reference centered in O. By summing RHS and LHS of the moment equilibrium equations for all particle in the unit cell and by dividing by the volume of the unit cell, one can write the following equation

$$\rho_{im}^\theta (\eta^{-1} \ddot{\omega}_m^0) = \frac{\eta}{V_0} \sum_I \sum_{F_I} A \frac{\partial w_i^{IJ}}{\partial \varepsilon_\alpha^0} \varepsilon_\alpha^1 \tag{35}$$

where $\rho_{im}^\theta = \sum_I \left[M_\theta^I \delta_{im} + M_u^I \varepsilon_{ijk} \varepsilon_{kmn} x_j^I x_n^I \right]/V_0$ is the tensor of inertia of the unit cell. By a lengthy algebraic manipulation, Eq. 35 can be rewritten as

$$\rho_{im}^\theta (\eta^{-1} \ddot{\omega}_m^0) = \frac{\eta}{2V_0} \sum_I \sum_{F_I} A \frac{\partial w_i^{IJ}}{\partial x_j} y_j^{IJ} \tag{36}$$

Replacing the definition of w^{IJ} in above equation and going through some more mathematical

derivations, the macroscale rotational equation of motion can finally be written as

$$\rho_{\theta ij} (\eta^{-1} \ddot{\omega}_j^0) = \varepsilon_{ijk} \sigma_{ij}^0 + \frac{\partial \mu_{ji}^0}{\partial x_j}$$
$$\mu_{ij}^0 = \frac{1}{2V_0} \sum_I \sum_{\mathcal{F}_I} A^{IJ} r t_\alpha^0 Q_{ij}^\alpha \tag{37}$$

where matrix Q_{ij}^α is difined as $Q_{ij}^\alpha = n_i^{IJ} \varepsilon_{jkl} c_k^I e_{\alpha l}^{IJ}$. Macroscopic stress tensor σ^0 is defined in 32. μ^0 is the macroscopic moment stress tensor calculated using results of RVE analysis.

3.3.2 Numerical results

In this section some preliminar numerical examples are presented to check the validity and accuracy of the derived formulation.

The elastic analysis of the RVE is considered first. The effective elastic material properties of a representative volume of concrete modeled by LDPM is studied. To carry out the elastic analysis, RVEs of six different sizes are considered, namely 10, 15, 20, 25, 35, 50 and 100 mm. The LDPM maximum particle size is chosen as 8 mm. For LDPM, the following elastic parameters are used: $E_N = 60273$ MPa and $E_T = 0.25 E_N$. For each size, five different particle configurations are considered and the homogenized elastic material properties are calculated for all of them.

To evaluate the Young modulus, a uniaxial macroscopic strain tensor is applied to the RVE. All components of the macroscopic strain tensor are zero except for the normal strain in one direction. The RVE problem subjected to this strain tensor is solved, and stress and moment stress tensors are calculated based on Eqs. 33 and 37. By interpreting the results through classical elasticity, one can calculate Young modulus and Poisson's ratio of the RVE. Figure 7a and b show the change in averaged Young modulus and Poisson's ratio with respect to RVE size. The length of the error bars at each size is equal to twice the standard deviation calculated over the five different realization for each RVE size.

One can see that both Young modulus and Poisson's ratio converge to a constant value by increasing the size of the RVE. Standard deviation of those quantities also tends to zero as size of the RVE is increased. This means also that the larger is the size of the RVE, the less the particle distribution inside the RVE affects the results.

The Cosserat character of LDPM is analyzed by applying a pure shear strain state to the RVE. Moment stress tensor and anti-symmetric part of the stress tensor are the quantities considered here. To investigate the effect of the size of the RVE on
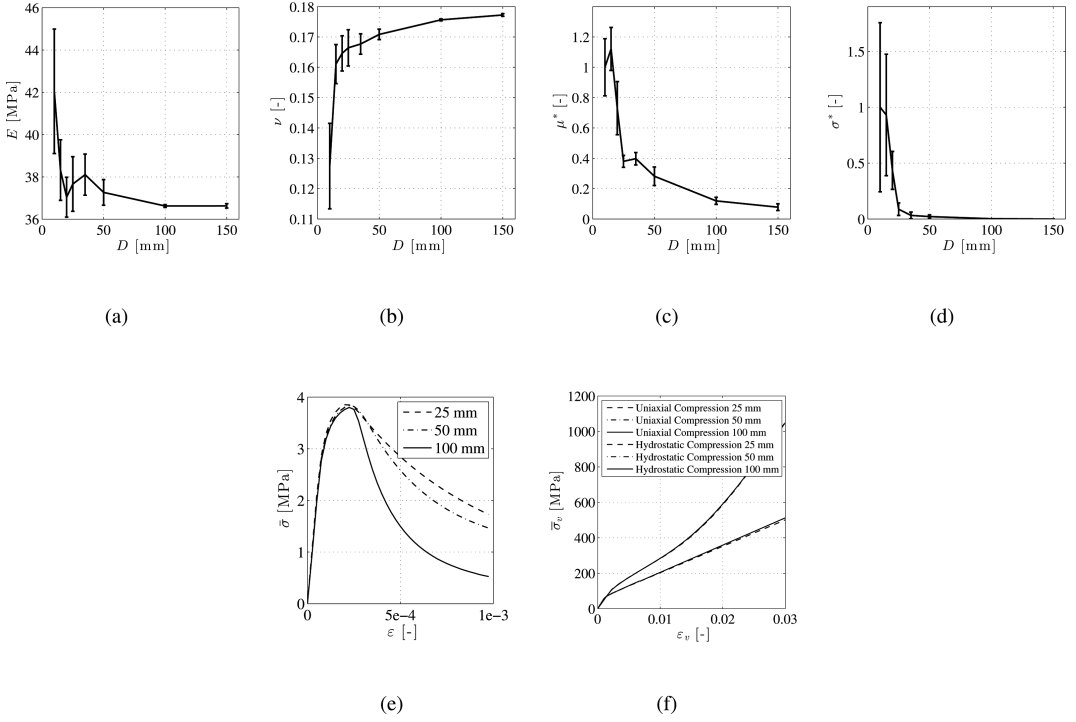
Figure 7. (a) Young modulus. (b) Poisson's ratio. (c) Magnitude of moment stress tensor. (d) Magnitude of anti-symmetric part of stress tensor. (e) Tensile stress-strain curve for 3 different RVE size. (f) Compressive stress-strain curve for 3 different RVE sizes.

these quantities, the following variables are defined with reference to the 10 mm size RVE:

$$\mu^* = \frac{\sqrt{\left[\sum_i \sum_j \mu_{ij}^2\right]_D}}{\sqrt{\left[\sum_i \sum_j \mu_{ij}^2\right]_{D=10}}} \tag{38}$$

$$\sigma^* = \frac{[\sigma_{21} - \sigma_{12}]_D}{[\sigma_{21} - \sigma_{12}]_{D=10}} \tag{39}$$

Variation of μ^* and σ^* with respect to RVE size is plotted in Figure 7c and d.

The plot shows that increasing the size of the RVE, while the maximum particle size is kept constant, the behavior of the homogenized continuum transitions from Cosserat-type to Cauchy-type as demonstrated by the decrease of the magnitude of moment stresstensor and anti-symmetric part of stress tensor. Similarly to the previous case, one can also notice that the standard deviation of these quantities also tends to zero by increasing the size of the RVE, which means, again, that the mesh configuration is less influential for large RVE sizes.

After the elastic analysis, the nonlinear response of RVEs of different size is investigated next. RVE sizes of 25, 50, and 100 mm are considered for these simulations. Seven different type of mesh configuration (particle distribution inside RVE) is considered for each RVE size. A uniaxial strain tensor is imposed on the RVEs while applying periodic boundary conditions. The homogenized stress-strain curves are obtained for each RVE and for each mesh configuration.

The average stress-strain curves are calculated for each RVE size and presented in Figure 7e. It is shown that increasing size of the RVE, forces the post peak curve to become steeper. This is consistent with the fact that the formulated homogenization procedure can capture strain localization as shown in Figure 8, where one can see the damaged RVEs at the end of tensile loading process. Contours in Figure 8 represent crack opening distributions for an imposed macroscopic strain equal to 0.001. While the ability of the homogenized procedure to handle damage localization is certainly a sign that the procedure captures well the overall behavior of the fine-scale model, it leaves open the question on how to select the size of the RVE. Similar to the
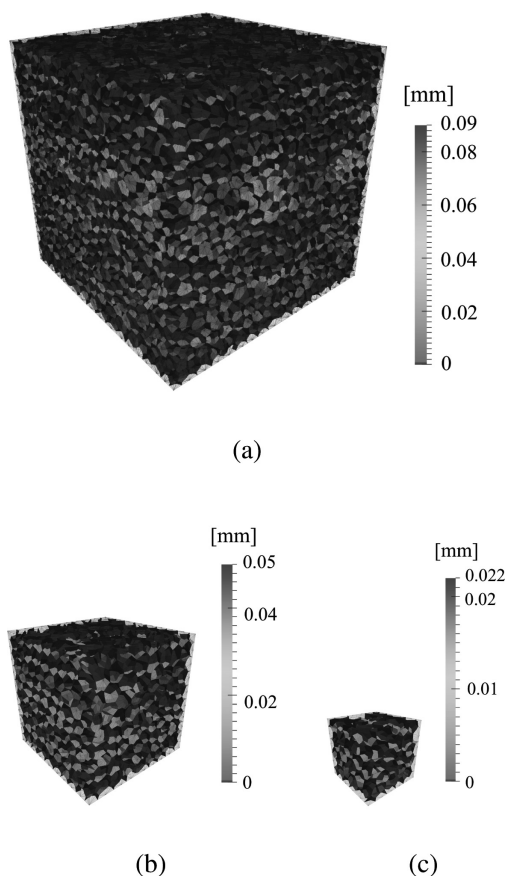
(a)

(b)   (c)

Figure 8.   Crack opening contours of damaged RVEs at tensile strain equal to 0.001.

work of Gitman and coworkes (Gitman et al. 2007) in the contest of computational homogenization, the current results suggest that objectivity of the macroscopic response under softening regime is preserved only if the volume of the RVE is equal to the macroscopic volume associated with the gauss point where the RVE is solved.

The response of the developed LDPM RVE is also investigated under compression. Two types of compression tests are considered: uniaxial strain (edometric) and hydrostatic compression tests. In uniaxial strain test, a strain tensor with a normal compressive component increasing up to 0.03 is considered. All other components of the strain tensor are set to zero. For the hydrostatic compression test, all normal components of the strain tensor increase from 0 to 0.03 (in compression), while the shear components are set to zero. According to the developed homogenization procedure, the strain tensor is projected over all facets of the RVE,

and homogenized response is calculated. For each RVE size, six different mesh configurations are considered. The results show that different mesh configurations affects the homogenized response only minimally. A change in the particle distribution within the RVE influences the results neither in elastic regime, nor in the nonlinear regime. This is the result of the fact that damage is distributed throughout the RVE under confined compression; therefore, damage localization does not occur. The average stress-strain response for different mesh realizations is also calculated and plotted for each RVE size in Figure 7f. Again, it is interesting to observe that the nonlinear compressive responses is independent on the RVE size.

3.3.3   Homohenization of ASR strain effects

Based on the results of the numerical study on the RVE (both elastic and nonlinear) response, one can conclude that the homogenization procedure can perfectly work for elastic cases and situations in which strain localization does not occur. To demonstrate this fact, the homogenization framework is used to study the effect of ASR expansion. In this case, damage is characterized by distributed cracking throughout the specimen and damage localization is not expected to occur. The reference LDPM solution is obtained by performing an accelerated ASR expansion simulation (Alnaggar et al. 2013) of a duration of 180 days. The simulated specimen is a 200-mm LDPM cube which is allowed to expand freely. Figure 9c shows the calculated crack distribution which demonstrate that strain localization does not occur under ASR expansion and, as expected, damage is relatively well distributed over the specimen volume.

The same simulation is then performed by using a 200 mm unrestrained hexahedral finite element with one Gauss point at which one RVE is attached as shown in Figure 9a. To study the effect of the RVE size, RVEs of 5 different sizes—namely 30,60, 90, 120 and 150 mm—are used in the simulations. During each time step, the finite element strain tensor is transferred to the RVE, and the homogenized stress tensor is calculated and transferred back to the finite element level for nodal forces and displacements calculation. The ASR strain is also applied at the RVE level (see Sec. 2.2). The volumetric strain of the finite element under free expansion is calculated for each RVE size and compared to the one of LDPM simulation and plotted in Figure 9b. As shown in Figure 9b, homogenization results are very close to the LDPM simulation even for small RVE sizes. It can be seen that the response is extremely accurate (and RVE size independent) in the initial period during which the response is elastic.

36
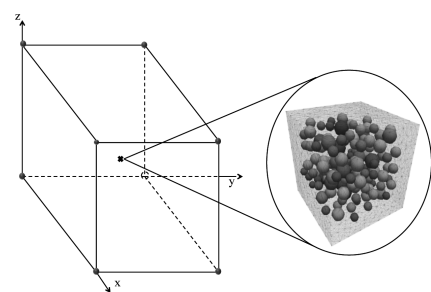
(a)
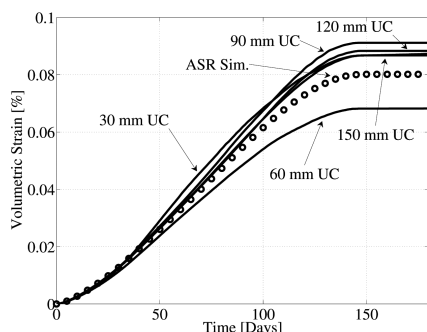
(b)
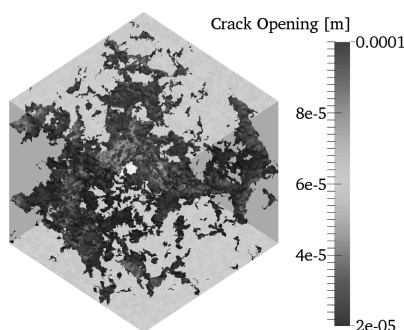
(c)

Figure 9. (a) Hexahedral finite element with an RVE assigned to its Gauss point. (b) Homogenized volumetric strain of the 200 mm finite element for different RVE sizes assigned to its Gauss point. (c) Damaged specimen under ASR strain effect.

The homogenized response of small RVE sizes deviate earlier from the LDPM simulation curves compared to the larger ones: this is mainly due to the significant effect of particle distribution for smaller RVEs. Finally, Figure 9b shows that

increasing the RVE size the homogenized response becomes closer and closer to the reference LDPM response. An accurate response (within 10% error) can be calculated by using a RVE of a very smaller size compared to the actual specimen with a significant reduction of the computational cost.

4 CLOSING REMARK

Concrete is a complex material and any significant future advancement in the description of its mechanical behavior depends on the ability of the scientific community to (1) formulate accurate and validated constitutive equations at various scales; (2) gathering complete sets of experimental data to be used for parameter identification and validation purposes; and (3) develop optimal multiscale methods to link the various scales allowing the accurate and efficient solution of large-scale problems by using fine-scale models. The results presented in this paper represent the first step towards pursuing this vision by adopting the Lattice Discrete Particle Model as fine-scale model.

Models and multiscale procedures presented in this paper are all implemented in MARS— Modeling and Analysis of the Response of Structures (Pelessone 2012)—a computational software recently developed by ES3.

REFERENCES

Alnaggar, M. & G. Cusatis (2012). Automatic parameter identification of discrete mesoscale models with application to the coarse-grained simulation of reinforced concrete structures. *20th Analysis and Computation Specialty Conference 36*, 406–417.

Alnaggar, M., G. Cusatis, & G. Di-Luzio (2013). Lattice discrete particle modeling (ldpm) of alkali silica reaction (asr) deterioration of concrete structures. *Cement and Concrete Composites 41*, 45–59.

Babuska, I. (1975). Homogenization and its application. Mathematical and computational problems. Numerical solution of partial differential equations. *III. Proc. Third Symp. (SYNSPADE), Univ. Maryland, College Park. 196*, 89–116.

Bažant, Z. & A. Steffens (2000). Mathematical model for kinetics of alkali-silica reaction in concrete. *Cement and Concrete Research 30*, 419–428.

Bažant, Z.P. & J. Planas (1998). *Fracture and size effect: in concrete and other quasibrittle materials*. CRC Press LLC.

Cusatis, G., A. Mencarelli, D. Pelessone, & J. Baylot (2011). Lattice discrete particle model (ldpm) for failure behavior of concrete. ii: Calibration and validation. *Cement and Concrete Composites 33*(9), 891–905.

Cusatis, G., D. Pelessone, & A. Mencarelli (2011). Lattice discrete particle model (ldpm) for concrete failure behavior of concrete. i: Theory. *Cement and Concrete Composites 33*(9), 881–890.

Cusatis, G. & Z. Xinwei (2013). High-order microplane theory for quasi-brittle materials with multiple characteristic lengths. *J. Eng. Mech.*

Emery, J., J. Hochalther, & A. Ingraffea (2007). Computational fracture mechanics of concrete structures: a retrospective through multiple lenses. In C. et al. (Ed.), *Fracture Mechanics of Concrete Structures New Trends in Fracture Mechanics of Concrete*, London, pp. 3–15. IA-FraMCoS: Taylor and Francis Group, London.

Farrell, D.E., H.S. Park, & W.K. Liu (2007). Implementation aspects of the bridging scale method and application to intersonic crack propagation. *Int. J. Numer. Meth. Eng. 71*(5), 583–605.

Fish, J., W. Chen, & R. Li. (2007). Generalized mathematical homogenization of atomistic media at finite temperatures in three dimensions. *Comput. Methods Appl. Mech. Engrg. 196*, 908–922.

Fish, J. & A. Wagiman. (1993). Multiscale finite element method for a locally nonperiodic heterogeneous medium. *Computational Mechanics. 12*, 164–180.

Gitman, I., H. Askes, & L. Sluys. (2007). Representative volume: Existence and size determination. *Engineering Fracture Mechanics 74*, 2518–2534.

Hassani, B. & E. Hinton (1998). A review of homogenization and topology optimization ihomogenization theory for media with periodic structure. *Computers and Structures. 69*, 707–717.

Pelessone, D. (2012). *MARS: Modeling and Analysis of the Response of Structures—User's Manual (http://www.es3inc.com/marssolver/)*. San Diego (CA), USA: ES3.

Schauffert, E. & G. Cusatis (2012). Lattice discrete particle model for fiber-reinforced concrete. i: Theory. *Journal of Engineering Mechanics 138*(7), 826–833.

Schauffert, E., G. Cusatis, D. Pelessone, J. ODaniel, & J. Baylot (2012). Lattice discrete particle model for fiber-reinforced concrete. ii: Tensile fracture and multiaxial loading behavior. *Journal of Engineering Mechanics 138*(7), 834–841.

Smith, J., G. Cusatis, D. Pelessone, E. Landis, J. O'Daniel, & J. Baylot (2014). Discrete modeling of ultra-high-performance concrete with application to projectile penetration. *International Journal of Impact Engineering 65*(0), 13–32.

Wagner, G.J., E.G. Karpov, & W.K. Liu (2004). Molecular dynamics boundary conditions for regular crystal lattices. *Comput. Meth. Appl. Mech. Eng. 193*(17), 1579–1601.

Wagner, G.J. & W.K. Liu (2003). Coupling of atomistic and continuum simulations using a bridging scale decomposition. *J. Comput. Phys. 190*(1), 249–274.